

# Self-consistent many-body metrology

Jae-Gyun Baak<sup>1</sup> and Uwe R. Fischer<sup>1</sup>

<sup>1</sup>*Seoul National University, Department of Physics and Astronomy,  
Center for Theoretical Physics, Seoul 08826, Korea*

(Dated: October 5, 2023)

We consider the classical and quantum metrology of interacting trapped bosons in a self-consistent many-body approach of the multiconfigurational Hartree type. Focusing on a tilted double-well geometry, we compare a self-consistently determined and monitored two-mode truncation, with dynamically changing orbitals, to the conventional two-mode interferometry of fixed orbitals, where only Fock space coefficients evolve in time. We demonstrate that, as a consequence, various metrological quantities of a concrete measurement such as the classical Fisher information and the maximum likelihood estimator are deeply affected by the orbitals' change during dynamical evolution. Self-consistency of the evolution of interacting trapped quantum gases thus fundamentally affects the interpretation of a given metrological protocol and its parameter estimation accuracy.

Within the currently emerging quantum era, quantum metrology [1–7] has proven itself to be a powerful tool for the accurate estimation of even very small physical parameters, such as gravitational wave amplitudes [8], or to limit the attainable measurement accuracy of fundamental constants such as the speed of light [9]. As a result, quantum metrology promises to revolutionize the existing technologies of measurement.

While quantum metrology has frequently been employed in the quantum optical context [10–12], more recently the corresponding experiments are also exploring coherent matter waves [13–26]. Photons freely propagating in the quantum vacuum are to a very good approximation noninteracting particles and are well described by plane waves of definite momentum. Matter waves forming Bose-Einstein condensates at very low temperatures are, however, interacting by the scattering of their elementary atomic or molecular constituents, and are spatially confined (trapped). In what follows, we show that the full self-consistency of the quantum many-body evolution of such a system needs in general to be taken into account, to yield reliable parameter estimation. We demonstrate that the interplay of Fock space amplitudes and time-dependent field operator modes (:= orbitals), the hallmark of self-consistent many-body evolution, is crucial. This interplay is not obtained when fixing the orbitals along the whole Hilbert space trajectory.

We take as an archetypical model system a tilted double well, where the parameter to be estimated is the linear tilt slope  $p_4$  (see Fig. 1). To facilitate comparison with conventional interferometry, we stay for the whole time evolution in an (explicitly verified) two-mode approximation, corresponding to two interferometric arms. We consider a simple (Mach-Zehnder type) experiment which counts at the instant of measurement the number of particles on the left and right. It is demonstrated, while a non-self-consistent evolution yields a null result for  $p_4$  [zero classical Fisher information (CFI)  $F_{p_4}$ ], that a self-consistent quantum many-body evolution yields finite CFI, thus enabling  $p_4$  estimation.

To determine the self-consistent evolution during the metrological protocol, we employ the multiconfigurational time-dependent Hartree (MCTDH) method [27–30]. The general  $N$ -body state is described by the ansatz

$$|\Psi(t)\rangle = \sum_{\vec{n}} C_{\vec{n}}(t) |\vec{n}(t)\rangle, \quad (1)$$

where  $\sum_{\vec{n}} |C_{\vec{n}}|^2 = 1$  for state normalization and  $\vec{n}$  denotes the set of occupation numbers in each mode (orbital),  $\{n_i | i = 1, 2, \dots, M\}$  with  $\sum_{i=1}^M n_i = N$ . The time-dependent Fock basis state  $|\vec{n}(t)\rangle$  indicates that the orbitals change in time as a result of finite  $M$  (see, Fig. 1), and their dynamics follows the system of nonlinear coupled integrodifferential Eqs. (S1) in the supplement [31]. Their numerical solution enables the precise determination of Fock space coefficients  $C_{\vec{n}}$  and orbitals at any time. We refer for further details to [30] for the MCTDH-

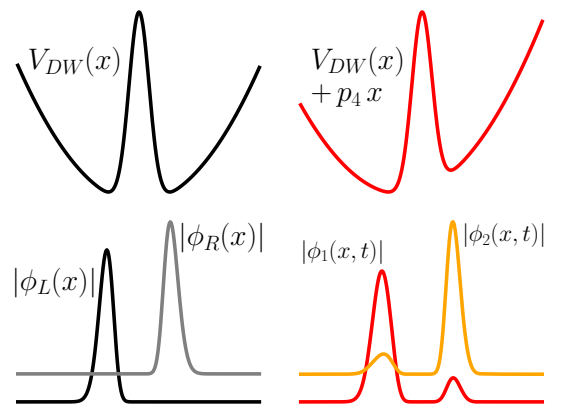


FIG. 1. Top: Trap potential. Left:  $t < 0$ , symmetric double well. Right: At  $t = 0$ , the tilt is switched on. Bottom: Initially localized orbitals in the large-barrier double-well potential self-consistently evolving in time after the potential tilt, and become delocalized, whereas without self-consistency they are assumed to remain localized. The orbitals are vertically offset for clarity.

X implementation used to solve Eqs. (S1) in [31].

The quantum metrological approach to parameter estimation cf. also, e.g., Refs. [32–36], proceeds essentially as follows. An initial state  $|\psi\rangle$  experiences a dynamical evolution, e.g.,  $e^{-i\hat{H}x t}$ , during the time  $t$  and the final state  $|\psi_X\rangle$  contains the information of the parameter  $X$ . One chooses an appropriate measurement on  $|\psi_X\rangle$ , to estimate  $X$ . Previous studies on quantum metrology with cold atoms cf., e.g., Refs. [13–26] have focused on the coefficients  $C_{\vec{n}}(X)$  in (1), and have calculated the quantum Fisher information  $\mathfrak{F}_{p_4}$  (QFI) from the set  $\{C_{\vec{n}}(X)\}$  only. However, since the orbitals also evolve by Eq. (S1) and the time evolution relies on  $X$ , the  $|\vec{n}(X)\rangle$  must be considered in the calculation of the QFI as well as the CFI. To evaluate the sensitivity of a quantum mechanical state to a parameter change however requires full exploitation of the information encoded in the state. Here, we make full use of the parameter dependence of the state, reflected in both coefficients and orbitals. We establish thereby numerically exact parameter estimation for trapped interacting quantum gases.

A bosonic gas with contact interactions trapped in a quasi-one-dimensional (quasi-1D) double-well potential is described by the Hamiltonian

$$\hat{H} = \sum_{j=1}^N \left\{ -\frac{1}{2} \frac{\partial^2}{\partial x_j^2} + V(x_j) \right\} + g \sum_{j < k} \delta(x_j - x_k) \quad (2)$$

in a dimensionless form, fixing a unit length  $L$  [37]. The quasi-1D interaction coupling  $g$  is assumed to be controllable by Feshbach or geometric scattering resonances and transverse trapping [38]. We assume  $V(x) = V_{DW}(x) + p_4 x = \frac{1}{2} p_1 x^2 + p_2 \exp(-x^2/(2p_3^2)) + p_4 x$  as the trap potential, where  $p_4 = 0$  initially, cf. Fig. 1. The other three parameters  $p_1 = 0.5$ ,  $p_2 = 50$ , and  $p_3 = 1$  are fixed to keep the validity of two-mode approximation throughout the dynamical evolution. The single-particle states are symmetric and antisymmetric states with respect to the origin, respectively, and addition and subtraction of them result in two well-localized orbitals: left  $\phi_L(x)$  and right  $\phi_R(x)$ , see Fig. 1. These orbitals, as approximate ground states of each well, are the basic one-particle states that furnish the two modes [39].

The estimation process of  $p_4$  proceeds as follows. An initial state represented in the form of Eq. (1) is supposed to be created. With  $\phi_L(x)$  and  $\phi_R(x)$ , we employ two coefficient distributions: A NOON (cat) state, which has  $|\psi_0\rangle = (|N, 0\rangle + |0, N\rangle)/\sqrt{2}$  and a spin coherent state  $|\psi_0\rangle = \sum_{k=0}^N \sqrt{\frac{N!}{k!(N-k)!}} \cos^{N-k}(\frac{\pi}{4}) \sin^k(\frac{\pi}{4}) |N-k, k\rangle$ . Then a small  $p_4$  is switched on, tilting trap potential tilted and making it asymmetric. The state then evolves according to Eq. (S1); finally, the number of particles in each well is measured and  $p_4$  is estimated from the set of measurement outcomes.

We are using two modes, i.e.,  $M = 2$ , for the self-consistent dynamics. As the interaction strength mea-

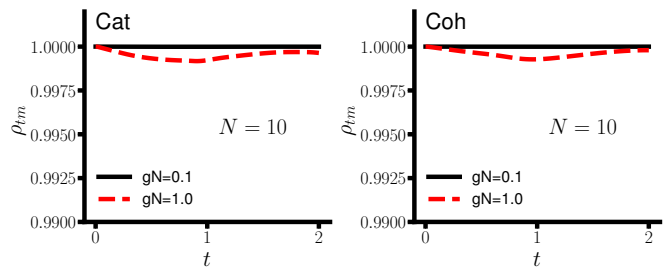


FIG. 2. Monitoring the two-mode truncation after  $p_4$  is turned on, by verifying whether  $\rho_{tm} = (\rho_1 + \rho_2)/N \lesssim 1$  (see text). Cat state (left) and spin coherent state (right). Black solid line is for  $gN = 0.1$  and red dashed line is for  $gN = 1$ .

sured by  $gN$ , representing a typical ratio of interaction over single-particle energies, increases, more modes are required to reproduce the many-body dynamics [40]. In order to adequately compare the SC results to those of the conventional SU(2) two-mode interferometry (TMI), which operates with the Fock space coefficients only, We maintain the validity of two-mode approximation throughout the time evolution, certifying its validity can be measured by  $\rho_{tm} := (\rho_1 + \rho_2)/N$ , cf. Fig. 2. Here,  $\rho_j$  are the  $j$ th largest eigenvalues of the reduced one-body density matrix  $\rho^{(1)}(x, x'; t)$  in Eq. (S2), which diagonalized reads  $\rho^{(1)}(x, x') = \sum_j \rho_j(t) \phi_j^{(no)*}(x', t) \phi_j^{(no)}(x, t)$  with the *natural orbitals*  $\{\phi_j^{(no)}(x, t) | j = 1, 2, \dots\}$ . When one  $\rho_1 = O(N)$  and the other  $\rho_j$  are not  $O(N)$ , one has a single condensate, and for more than one  $\rho_j$  of  $O(N)$ , we have a fragmented condensate [41]. The validity of the two-mode approximation (that the condensate is two-fold fragmented) depends on the extent to which  $\rho_1 \simeq \rho_2 \simeq O(N/2)$  and  $\rho_{tm} \simeq O(1)$  hold.

To define an initial state, we used four orbitals ( $M = 4$ ), including  $\phi_L(x)$  and  $\phi_R(x)$ , and monitored the natural occupations  $\rho_j$  while the state evolves in time self-consistently under nonzero  $p_4$ , for both cat and spin coherent state. Fig. 2 shows the monitoring of  $\rho_{tm}$ , where we observe it is close to unity. Also, both  $\rho_1$  and  $\rho_2$  are macroscopically occupied during the evolution, with negligible occupation of  $\rho_3$  and  $\rho_4$ . This fact however also depends on the parameter regime used. When  $gN = 0.1$ , two modes are sufficient, but when  $gN = 1$ ,  $\rho_{tm}/N$  discernibly dips below unity. Furthermore, increasing  $p_4$ ,  $\rho_{tm}$  increasingly deviates from unity and the two-mode approximation fails. An appropriate regime of parameters where  $\rho_{tm} \simeq 1$  is obtained when we fix  $gN = 0.1$  and  $p_4 = 0.1$ . Also, even though the natural orbitals are used in the discussion above, we can apply the two-mode criterion to the left/right orbitals or their time-evolved forms, i.e.,  $\phi_1(x, t)$  and  $\phi_2(x, t)$ , since there always exists a unitary transformation such that  $\phi_j(x, t) = \sum_{jk} U_{jk} \phi_k^{(no)}(x, t)$ . When two natural orbitals are sufficient, this guarantees that the number of other unitarily transformed orbitals is two as well.

When the second-quantized form of Eq. (2) is two-mode expanded with  $\hat{\Psi}(x) = \hat{b}_L \phi_L(x) + \hat{b}_R \phi_R(x)$ , a two-site single-band Bose-Hubbard model Hamiltonian is obtained. In terms of the usual SU(2) Pauli matrices  $\hat{J}_x = \frac{1}{2}(\hat{b}_L \hat{b}_R + \hat{b}_R^\dagger \hat{b}_L^\dagger)$ ,  $\hat{J}_z = \frac{1}{2}(\hat{b}_L \hat{b}_L - \hat{b}_R^\dagger \hat{b}_R)$ ,

$$\hat{H} = -\tau \hat{J}_x + \epsilon \hat{J}_z + U \hat{J}_z^2, \quad (3)$$

where  $\tau$  is tunneling amplitude,  $\epsilon$  indicates an energy offset between wells, and  $U \propto g$  is the interaction coupling, all of which depend on integrals involving the two orbitals. The implementation of quantum metrological protocols using the above Hamiltonian was carried out, e.g., in Refs. [18, 20, 36]. An initial state  $|\psi_0\rangle$ , therein completely defined by the distribution of coefficients  $C_{\vec{n}}$ , evolves as  $\exp(-i\hat{H}t)|\psi_0\rangle$ , and the parameter of interest, e.g.,  $\epsilon$ , is estimated from the population imbalance between the two modes [18, 20, 23]. In our setup, the strong barrier renders the initial  $\tau$  exponentially small compared to  $\epsilon$  and  $U$ , and  $\epsilon \neq 0$ , as the symmetry of  $V(x)$  is broken by  $p_4$ . Hence the TMI time evolution operator is, to very good accuracy,  $\exp(-i(\epsilon \hat{J}_z + U \hat{J}_z^2)t)$ , and the quantum Fisher information (QFI) can be analytically calculated by  $\mathfrak{F}_\epsilon = 4 \langle \psi_0 | (\Delta \hat{J}_z)^2 | \psi_0 \rangle$ . When the cat state is used,  $\mathfrak{F}_\epsilon = N^2 t^2$ , which is denoted as the Heisenberg limit. For the spin coherent state,  $\mathfrak{F}_\epsilon = N \sin^2(\theta) t^2$ , which represents the shot-noise limit (the so-called standard quantum limit). Any nonzero  $\tau$  deteriorates the  $N$ -scaling of  $\mathfrak{F}_\epsilon$  [18], which can be confirmed by numerically calculating the QFI. Note that here only the change of Fock space coefficients has been considered, while the orbital basis is fixed in TMI. Because of the latter fact, the still exponentially small  $\tau$  and  $U$  are kept constant during the evolution, and  $\epsilon$  is abruptly switched on at  $t = 0$ . In our setting,  $\epsilon \in (-0.7, -0.6)$ , and  $U \in (0.002, 0.03)$ , with concrete values as a function of  $gN$  and  $N$ , on which in turn the initial orbitals  $\phi_L(x)$  and  $\phi_R(x)$  depend). Recall that our target parameter is  $p_4$ , not  $\epsilon$ , thus by using the chain rule,  $\mathfrak{F}_{p_4} = \mathfrak{F}_\epsilon \times (h_1 - h_2)^2$ , where the single-particle energies  $h_i := \int dx \phi_i^*(x) \left[ -\frac{1}{2} \frac{\partial^2}{\partial x^2} + V(x) \right] \phi_i(x)$ .

First, we compare the QFIs of the SC approach and the conventional TMI. The QFI with respect to a given parameter  $X$  inscribed onto a pure state  $|\psi_X\rangle$ , is  $\mathfrak{F}_X = 4(\langle \partial_X \psi_X | \partial_X \psi_X \rangle - |\langle \psi_X | \partial_X \psi_X \rangle|^2)$ , and insertion of Eq. (1) into  $|\psi_X\rangle$  gives Eq., (S4), which facilitates calculation of the QFI using the ingredients of MCTDH theory from the expansion (1). The first row in Fig. 3 shows the QFI versus time  $t$  or the number of particles  $N$ . For each initial state, the SC method reproduces very well the QFI predicted by TMI. The influence of self-consistency thus plays a subdominant role for  $\mathfrak{F}_X$ , as the latter completely depends on the final state itself, and the self-consistency (changing orbitals), essentially represents fitting that state more exactly. When the bosons weakly interact ( $gN = 0.1$ ) and the disturbance to the system is small ( $p_4 = 0.1$ ), conventional TMI therefore

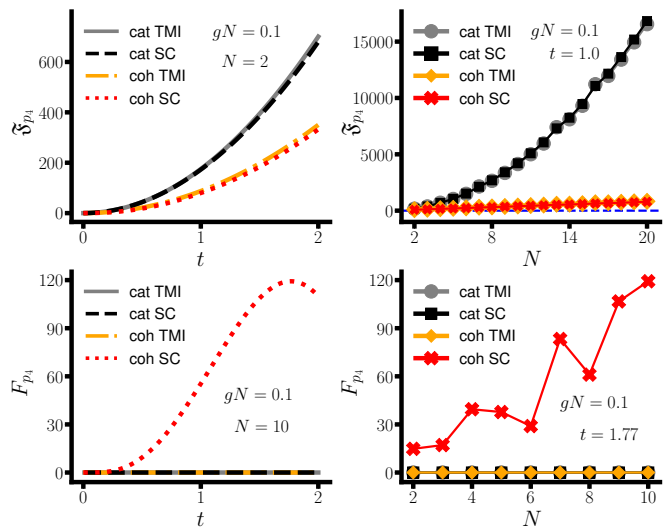


FIG. 3. First and second row display quantum ( $\mathfrak{F}$ ) and classical (F) Fisher information, respectively, plotted versus time  $t$  (left) and particle number  $N$  (right), for cat and coherent (coh) states, respectively. “TMI” denotes the conventional two-mode interferometry, and “SC” stands for the self-consistent approach. At the maximum on the lower left plot, at  $t = 1.77$ , the tunneling amplitude in the SC evolution has increased to  $\tau \simeq 0.09$  (for  $N = 10$ ).

approximates well the QFI. We have verified in this regard that terms consisting of Fock space coefficients only, and those involving orbitals, in the general relation for  $\mathfrak{F}_X$  Eq. (S4) tend to compensate each other.

We now turn to the classical Fisher information (CFI), associated to a concrete measurement, for which the impact of self-consistency becomes manifest. Since counting the number of bosons in each well constitutes our measurement, the corresponding CFI is defined as

$$F_{p_4} = \sum_{\vec{n}} P(\vec{n}|p_4) \left( \frac{\partial \log P(\vec{n}|p_4)}{\partial p_4} \right)^2, \quad (4)$$

where  $P(\vec{n}|p_4)$  is the probability distribution of the measurement outcomes  $\vec{n} = (n_L, n_R)$ , given  $p_4$ , and  $n_L$  and  $n_R$  are the numbers of particles that reside in the left and the right well, respectively. An appropriate  $P(\vec{n}|p_4)$  has to be constructed to calculate the CFI and the conventional TMI approach considers that  $P(\vec{n}|p_4) := |\langle \vec{n}(t) | \Psi(t) \rangle|^2$ . Then, the CFI *always exactly vanishes*, irrespective of the initial state, as the Hamiltonian contains only  $\hat{J}_z$  and  $\hat{J}_z^2$ . The corresponding TMI time evolution therefore just changes the phases of the coefficients:  $C_k(t) = \exp(-i\epsilon \frac{N-2k}{2} t) \exp(-iU(\frac{N-2k}{2})^2 t) C_k(0)$ , where  $|\psi(t)\rangle = \sum_{k=0}^N C_k(t) |N-k, k\rangle = \exp(-i(\epsilon \hat{J}_z + U \hat{J}_z^2)t) |\psi(0)\rangle$  and  $\hat{J}_z |N-k, k\rangle = \frac{N-2k}{2} |N-k, k\rangle$ . Then  $P(\vec{n} = (N-k, k) | p_4) = |C_k(t)|^2 = |C_k(0)|^2$ , independent of  $p_4$ , yielding vanishing CFI for  $p_4$  in the TMI approach.

On the other hand, when the orbitals evolve together with the Fock space coefficients in the SC framework, the

initial interpretation of the orbitals cannot be maintained throughout the time evolution. Initially well-localized orbitals, i.e.,  $\phi_L(x) = \phi_1(x, 0)$  and  $\phi_R(x) = \phi_2(x, 0)$ , correspond to a particle being found in the left and right well is regarded as belonging  $\phi_L(x)$  and  $\phi_R(x)$ , respectively. However, the orbitals change with time during the many-body evolution, thus the orbitals at a later time, i.e.,  $\phi_1(x, t)$  and  $\phi_2(x, t)$ , do not necessarily imply left or right localization at a given time of measurement. Therefore, simply computing  $P(\vec{n}) = |\langle \vec{n}(t) | \Psi(t) \rangle|^2$ , as in the TMI approach, is not applicable. In the bosonic field operator  $\hat{\Psi}(x) = \sum_j \hat{b}_j(t) \phi_j(x, t)$ , it is clear that the bosonic annihilation operator  $\hat{b}_j(t)$  corresponds to the time-evolving orbital  $\phi_j(x, t)$ , which may lose its localization at some time  $t$  as shown in Fig. 1. In conclusion, the Fock state in Eq. (1)

$$|\vec{n}(t)\rangle = \frac{(\hat{b}_1^\dagger(t))^{n_1} (\hat{b}_2^\dagger(t))^{n_2} \cdots (\hat{b}_M^\dagger(t))^{n_M}}{\sqrt{n_1! n_2! \cdots n_M!}} |0\rangle \quad (5)$$

cannot by itself appropriately project the quantum state into any of  $|\vec{n}\rangle$  and  $\langle \vec{n}(t) | \Psi(t) \rangle$  cannot be interpreted as the probability amplitude for each measurement outcome as in TMI. In other words,  $|\vec{n}(t)\rangle$  and  $|\vec{n}\rangle$  are different in the SC approach. Hence it is necessary to re-establish a connection between time-evolving orbitals and  $|\vec{n}\rangle$  that corresponds to a measurement outcome, resulting in the proper distribution  $P(\vec{n}) = |\langle \vec{n} | \Psi(t) \rangle|^2 \neq |\langle \vec{n}(t) | \Psi(t) \rangle|^2$ .

In the SC time evolution after the trap potential is tilted,  $\phi_1(x, t)$  and  $\phi_2(x, t)$  remain well-localized in the case of a cat state. That is,  $\phi_1(x, t)$  ( $\phi_2(x, t)$ ) begins from  $\phi_1(x, 0) = \phi_L(x)$  [ $\phi_2(x, 0) = \phi_R(x)$ ] and their absolute value remains nearly identical except slightly wider (narrower) width and shorter (taller) height, respectively. For the spin coherent state, however,  $\phi_1(x, t)$  and  $\phi_2(x, t)$  spread into opposite wells while they evolve under nonzero  $p_4$ ; see Fig. 1. Then even when a particle resides in  $\phi_1(x, t)$  or  $\phi_2(x, t)$ , to assign it to the left or right well is ambiguous. One can however still define mathematically “left” or “right” by integrating the orbitals from  $-\infty$  to the center point  $x = 0$  of  $V(x)$  and from the center point of  $V(x)$  to  $\infty$ , respectively:  $P_{\text{Left}} = \int_{-\infty}^0 |\phi_j(x, t)|^2 dx$  and  $P_{\text{Right}} = \int_0^{\infty} |\phi_j(x, t)|^2 dx$ . One can construct the correct  $P(\vec{n}|p_4)$  by computing the permanent of a special matrix composed from  $P_{\text{Right}}$  and  $P_{\text{Left}}$ , which limits the computable range of  $N$  due to rapidly increasing algorithmic complexity [31].

The second row in Fig. 3 shows the CFI versus  $t$  or  $N$ . The conventional approach with fixed orbitals results in vanishing CFI, as expected. Also, even though the SC approach is used, the cat state shows almost vanishing CFI, which is attributed to the fact that the orbitals stay localized in each well during the whole evolution time and the probabilities, i.e.,  $P_{\text{Left}}$  and  $P_{\text{Right}}$ , remain nearly constant (for small  $p_4$ ). Thus under the given measurement the change of  $P(\vec{n}|p_4)$  with respect to  $p_4$

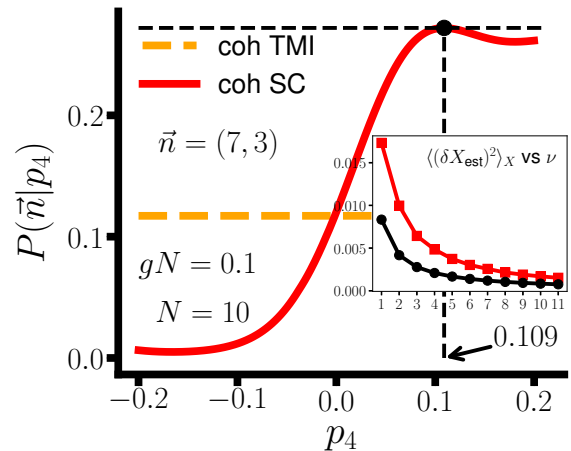


FIG. 4. Shown is a single implementation of the MLE for an estimate of  $p_4$  using the spin coherent state. Red solid line is for the SC approach and orange dashed line (a constant  $\forall p_4$  shown) for the TMI. In the inset, red square is the mean-square deviation and black round is the Cramér-Rao lower bound from Eq. (6).

is negligible. However, the spin coherent state displays a significant change in orbitals and displays increasing CFI during the early stage of time evolution. Bottom right in Fig. 3 shows the  $N$ -scaling of the CFI, and here the SC approach with spin coherent state shows an almost linearly increasing CFI. The complex fluctuation pattern appears because of the short time  $t = 1.77$  after a nonzero  $p_4$  is suddenly applied and as the measurement time  $t$  increases these fluctuations smoothen out. Thus the SC approach may yield drastically different metrological predictions from a TMI based method.

Fig. 4 shows our primary result: The implementation of parameter estimation in the final stage of the metrological protocol. The maximum likelihood estimator (MLE) [5] is used as a concrete example here, because it asymptotically saturates the Cramér-Rao bound [3]

$$\langle (\delta X_{\text{est}})^2 \rangle_X \geq \frac{1}{\nu F_X}, \quad (6)$$

where  $X$  here is  $p_4$ ,  $X_{\text{est}}$  is an estimator of  $X$ , and the deviation is  $\delta X_{\text{est}} := X_{\text{est}} / |\partial \langle X_{\text{est}} \rangle_X / \partial X| - X$ . In Fig. 4, the likelihood function  $P(\vec{n}|p_4)$  is displayed supposing, for concreteness, that the measurement outcome is  $\vec{n} = (n_L, n_R) = (7, 3)$ , where  $n_L$  and  $n_R$  denote the number of particles found in left and right well, respectively. The red solid line shows the maximum of  $P(\vec{n}|p_4)$  at  $p_4 \simeq 0.109$ , thus the estimate of  $p_4$  given  $\vec{n} = (7, 3)$  is  $X_{\text{est}} \simeq 0.109$ . Similarly, every single outcome, 11 in total, is matched with a corresponding estimate of  $p_4$ . The orange dashed line that corresponds to the result of the conventional TMI approach with a spin coherent state stays flat, which means that the information given by the measurement outcome  $\vec{n} = (7, 3)$  is zero, so one cannot extract an estimate of  $p_4$ , in accordance with  $F_{p_4} = 0$ .

The MLE is in general not unbiased. Unbiasedness is assessed by  $\langle X_{\text{est}} \rangle_X$ , in which the bracket is the average with respect to  $P(\vec{n}|p_4)$ . When  $\langle X_{\text{est}} \rangle_X = X$  holds, the estimator is unbiased. In our current example, this is approximately fulfilled near  $p_4 = 0$ , but it fails with increasing  $p_4$ . For instance, in Fig. 4, the true value of  $p_4$  is 0.1 and the MLE is slightly biased such that  $\langle X_{\text{est}} \rangle_{X=0.1} \simeq 0.11$ . Also,  $\partial \langle X_{\text{est}} \rangle_X / \partial X|_{X=0.1} \simeq 0.6$ , which enables to calculate the mean-square deviation  $\langle (\delta X_{\text{est}})^2 \rangle_{X=0.1}$ . The inset in Fig. 4 verifies, asymptotically, as it should, the mean-square deviation approaches the Cramér-Rao lower bound, for an increasing number  $\nu$  of measurement outcomes to obtain a single estimate ( $\nu$  appears in Eq. (6) due to the central limit theorem). The asymptotic saturation of Eq. (6) by the MLE implies that equality in the bound is attained when  $\nu \rightarrow \infty$  [31].

In conclusion, we have found using a self-consistent many-body approach that the metrological outcome of a specific measurement utilizing interacting confined bosons needs to conform to the final self-consistently computed state. On one hand, the QFI completely depends on the parameter dependence of the final state itself, and is relatively unaffected by self-consistency (in the weakly interacting regime). On the other, even in the latter regime, the CFI for a concrete parameter estimation experiment, as we have shown, can be strongly affected by self-consistency due to its sensitive dependence on the orbitals' time evolution. We infer that metrology with ultracold quantum gases in general requires the self-consistency of dynamical evolution to correctly predict the estimation precision that can be accomplished in a given metrological protocol.

This work has been supported by the National Research Foundation of Korea under Grants No. 2017R1A2A2A05001422 and No. 2020R1A2C2008103.

- 
- [1] C. W. Helstrom, Minimum mean-squared error of estimates in quantum statistics, *Physics Letters A* **25**, 101 (1967).
- [2] C. W. Helstrom, Quantum detection and estimation theory, *Journal of Statistical Physics* **1**, 231 (1969).
- [3] S. L. Braunstein and C. M. Caves, Statistical distance and the geometry of quantum states, *Phys. Rev. Lett.* **72**, 3439 (1994).
- [4] V. Giovannetti, S. Lloyd, and L. Maccone, Quantum Metrology, *Phys. Rev. Lett.* **96**, 010401 (2006).
- [5] H. Wiseman and G. Milburn, *Quantum Measurement and Control* (Cambridge University Press, 2010).
- [6] G. Tóth and I. Apellaniz, Quantum metrology from a quantum information science perspective, *Journal of Physics A: Mathematical and Theoretical* **47**, 424006 (2014).
- [7] D. Braun, G. Adesso, F. Benatti, R. Floreanini, U. Marzolino, M. W. Mitchell, and S. Pirandola, Quantum-enhanced measurements without entanglement, *Rev. Mod. Phys.* **90**, 035006 (2018).
- [8] R. Schnabel, N. Mavalvala, D. E. McClelland, and P. K. Lam, Quantum metrology for gravitational wave astronomy, *Nature Communications* **1**, 121 (2010).
- [9] D. Braun, F. Scheiter, and U. R. Fischer, Intrinsic measurement errors for the speed of light in vacuum, *Classical and Quantum Gravity* **34**, 175009 (2017).
- [10] V. Giovannetti, S. Lloyd, and L. Maccone, Advances in quantum metrology, *Nature Photonics* **5**, 222 (2011).
- [11] E. Polino, M. Valeri, N. Spagnolo, and F. Sciarrino, Photonic quantum metrology, *AVS Quantum Science* **2**, 024703 (2020).
- [12] M. Barbieri, Optical Quantum Metrology, *PRX Quantum* **3**, 010202 (2022).
- [13] L. Pezzè, L. A. Collins, A. Smerzi, G. P. Berman, and A. R. Bishop, Sub-shot-noise phase sensitivity with a Bose-Einstein condensate Mach-Zehnder interferometer, *Phys. Rev. A* **72**, 043612 (2005).
- [14] S. Choi and B. Sundaram, Bose-Einstein condensate as a nonlinear Ramsey interferometer operating beyond the Heisenberg limit, *Phys. Rev. A* **77**, 053613 (2008).
- [15] S. Boixo, A. Datta, M. J. Davis, A. Shaji, A. B. Tacla, and C. M. Caves, Quantum-limited metrology and Bose-Einstein condensates, *Phys. Rev. A* **80**, 032103 (2009).
- [16] C. Gross, Spin squeezing, entanglement and quantum metrology with Bose-Einstein condensates, *Journal of Physics B: Atomic, Molecular and Optical Physics* **45**, 103001 (2012).
- [17] J. Chwedeñczuk, F. Piazza, and A. Smerzi, Phase estimation with interfering Bose-Einstein-condensed atomic clouds, *Phys. Rev. A* **82**, 051601 (2010).
- [18] J. Javanainen and H. Chen, Optimal measurement precision of a nonlinear interferometer, *Phys. Rev. A* **85**, 063605 (2012).
- [19] W. Muessel, H. Strobel, D. Linnemann, D. B. Hume, and M. K. Oberthaler, Scalable Spin Squeezing for Quantum-Enhanced Magnetometry with Bose-Einstein Condensates, *Phys. Rev. Lett.* **113**, 103004 (2014).
- [20] K. Gietka and J. Chwedeñczuk, Atom interferometer in a double-well potential, *Phys. Rev. A* **90**, 063601 (2014).
- [21] S. Ragole and J. M. Taylor, Interacting Atomic Interferometry for Rotation Sensing Approaching the Heisenberg Limit, *Phys. Rev. Lett.* **117**, 203002 (2016).
- [22] C. Luo, J. Huang, X. Zhang, and C. Lee, Heisenberg-limited Sagnac interferometer with multiparticle states, *Phys. Rev. A* **95**, 023608 (2017).
- [23] B. J. Dalton, Two-mode theory of BEC interferometry, *Journal of Modern Optics* **54**, 615 (2007).
- [24] J. Czajkowski, K. Pawłowski, and R. Demkowicz-Dobrzański, Many-body effects in quantum metrology, *New Journal of Physics* **21**, 053031 (2019).
- [25] J. Huang, S. Wu, H. Zhong, and C. Lee, Quantum metrology with cold atoms, in *Annual Review of Cold Atoms and Molecules* (2014) Chap. 7, pp. 365–415.
- [26] L. Pezzè, A. Smerzi, M. K. Oberthaler, R. Schmied, and P. Treutlein, Quantum metrology with nonclassical states of atomic ensembles, *Rev. Mod. Phys.* **90**, 035005 (2018), and references therein.
- [27] A. I. Streltsov, O. E. Alon, and L. S. Cederbaum, General variational many-body theory with complete self-consistency for trapped bosonic systems, *Phys. Rev. A* **73**, 063626 (2006).

- [28] O. E. Alon, A. I. Streltsov, and L. S. Cederbaum, Multiconfigurational time-dependent Hartree method for bosons: Many-body dynamics of bosonic systems, *Phys. Rev. A* **77**, 033613 (2008).
- [29] A. U. J. Lode, C. Lévêque, L. B. Madsen, A. I. Streltsov, and O. E. Alon, Colloquium: Multiconfigurational time-dependent Hartree approaches for indistinguishable particles, *Rev. Mod. Phys.* **92**, 011001 (2020).
- [30] R. Lin, P. Mognini, L. Papariello, M. C. Tsatsos, C. Lévêque, S. E. Weiner, E. Fasshauer, R. Chitra, and A. U. J. Lode, MCTDH-X: The multiconfigurational time-dependent Hartree method for indistinguishable particles software, *Quantum Science and Technology* **5**, 024004 (2020).
- [31] See the Supplemental Material, which quotes Refs. [42-44], for an extended discussion and details on the implementation of the MCDTH method for the present metrological purposes. Equation numbers in the format (S#) refer to equations in the Supplemental Material.
- [32] A. Fujiwara and H. Nagaoka, Quantum Fisher metric and estimation for pure state models, *Physics Letters A* **201**, 119 (1995).
- [33] O. E. Barndorff-Nielsen and R. D. Gill, Fisher information in quantum statistics, *Journal of Physics A: Mathematical and General* **33**, 4481 (2000).
- [34] S. Boixo, A. Datta, S. T. Flammia, A. Shaji, E. Bagan, and C. M. Caves, Quantum-limited metrology with product states, *Phys. Rev. A* **77**, 012317 (2008).
- [35] S. Alipour, M. Mehboudi, and A. T. Rezakhani, Quantum Metrology in Open Systems: Dissipative Cramér-Rao Bound, *Phys. Rev. Lett.* **112**, 120405 (2014).
- [36] T. Wasak, A. Smerzi, L. Pezzè, and J. Chwedeńczuk, Optimal measurements in phase estimation: simple examples, *Quantum Information Processing* **15**, 2231 (2016).
- [37] In  $^{87}\text{Rb}$ ,  $L = 1 \mu\text{m}$  yields a time unit  $\Delta t = 1.366$  msec.
- [38] M. Olshani, Atomic Scattering in the Presence of an External Confinement and a Gas of Impenetrable Bosons, *Phys. Rev. Lett.* **81**, 938 (1998).
- [39] G. J. Milburn, J. Corney, E. M. Wright, and D. F. Walls, Quantum dynamics of an atomic Bose-Einstein condensate in a double-well potential, *Phys. Rev. A* **55**, 4318 (1997).
- [40] O. E. Alon and L. S. Cederbaum, Pathway from Condensation via Fragmentation to Fermionization of Cold Bosonic Systems, *Phys. Rev. Lett.* **95**, 140402 (2005).
- [41] O. Penrose and L. Onsager, Bose-Einstein Condensation and Liquid Helium, *Phys. Rev.* **104**, 576 (1956).
- [42] K.-S. Lee and U. R. Fischer, Truncated many-body dynamics of interacting bosons: A variational principle with error monitoring, *International Journal of Modern Physics B* **28**, 1550021 (2014).
- [43] A. Nijenhuis and H. Wilf, *Combinatorial Algorithms: For Computers and Calculators*, edited by W. Rheinboldt, Computer science and applied mathematics (Elsevier Science, 2014).
- [44] X. Niu, S. Su, and J. Zheng, A New Fast Computation of a Permanent, *IOP Conference Series: Materials Science and Engineering* **790**, 012057 (2020).

SUPPLEMENTAL MATERIAL

Multiconfigurational time-dependent Hartree theory

Given a set of coefficients and a set of orbitals for an initial state, the time evolution in the MCTDH framework proceeds according to the following system of equations:

$$\begin{aligned} i \frac{\partial \mathbf{C}(t)}{\partial t} &= \mathbf{H}(t) \mathbf{C}(t), \\ i \partial_t |\phi_j\rangle &= \hat{P} \left[ \hat{h} |\phi_j\rangle + \sum_{k,s,q,l} [\rho^{-1}]_{jk} \rho_{ksql} \hat{W}_{sl} |\phi_q\rangle \right], \end{aligned} \quad (\text{S1})$$

which is derived by applying the time-dependent variational principle to the interacting  $N$ -body Hamiltonian  $\hat{H} = \sum_{j=1}^N \hat{h}(x_j) + \sum_{j<k} \hat{W}(x_j - x_k)$  [28]. Here,  $\mathbf{C}(t)$  is a column vector that consists of all possible expansion coefficients  $C_{\bar{n}}(t)$  and  $\mathbf{H}(t)$  corresponds to the time-dependent Hamiltonian matrix in the basis  $\{|\bar{n}(t)\rangle\}$ . Also,  $\hat{h}$  is a single-particle Hamiltonian,  $\hat{W}_{sl} = \int dx' \phi_s^*(x') \hat{W}(x - x') \phi_l(x')$ , and  $\hat{P} = 1 - \sum_{j=1}^M |\phi_j\rangle \langle \phi_j|$  is an projection operator to the subspace that is orthogonal to the one spanned by orbitals. The  $[\rho^{-1}]_{jk}$  is a matrix element of the inverse of reduced one-body density matrix:

$$\begin{aligned} \rho(x, x'; t) &= \langle \Psi(t) | \hat{\Psi}^\dagger(x') \hat{\Psi}(x) | \Psi(t) \rangle \\ &= \sum_{k,q} \phi_k^*(x', t) \phi_q(x, t) \langle \Psi(t) | \hat{b}_k^\dagger(t) \hat{b}_q(t) | \Psi(t) \rangle \\ &= \sum_{k,q} \phi_k^*(x', t) \phi_q(x, t) \rho_{kq}(t), \end{aligned} \quad (\text{S2})$$

where the  $\rho_{kq}$  is, for the cases of  $k = q$  and  $k \neq q$ ,

$$\rho_{kk} = \sum_{\bar{n}} |C_{\bar{n}}(t)|^2 n_k, \quad \rho_{kq} = \sum_{\bar{n}} C_{\bar{n}}^*(t) C_{\bar{n}_k^q}(t) \sqrt{n_k(n_q + 1)}.$$

Similarly,  $\rho_{ksql}$  is a matrix element of the reduced two-body matrix

$$\begin{aligned} \rho(x_1, x_2, x'_1, x'_2; t) &= \langle \Psi(t) | \hat{\Psi}^\dagger(x'_1) \hat{\Psi}^\dagger(x'_2) \hat{\Psi}(x_1) \hat{\Psi}(x_2) | \Psi(t) \rangle \\ &= \sum_{k,s,q,l} \phi_k^*(x'_1, t) \phi_s^*(x'_2, t) \phi_q(x_1, t) \phi_l(x_2, t) \rho_{ksql}(t), \end{aligned} \quad (\text{S3})$$

where

$$\begin{aligned} \rho_{kkkk} &= \sum_{\bar{n}} |C_{\bar{n}}(t)|^2 n_k(n_k - 1), \quad \rho_{kssk} = \sum_{\bar{n}} |C_{\bar{n}}(t)|^2 n_k n_s, \\ \rho_{kkqq} &= \sum_{\bar{n}} C_{\bar{n}}^*(t) C_{\bar{n}_{kk}^{qq}}(t) \sqrt{(n_k - 1)n_k(n_q + 1)(n_q + 2)}, \quad \rho_{kkkl} = \sum_{\bar{n}} C_{\bar{n}}^*(t) C_{\bar{n}_k^l}(t) (n_k - 1) \sqrt{n_k(n_l + 1)}, \\ \rho_{ksss} &= \sum_{\bar{n}} C_{\bar{n}}^*(t) C_{\bar{n}_s^s}(t) n_s \sqrt{n_k(n_s + 1)}, \quad \rho_{kkql} = \sum_{\bar{n}} C_{\bar{n}}^*(t) C_{\bar{n}_{kk}^{ql}}(t) \sqrt{(n_k - 1)n_k(n_q + 1)(n_l + 1)}, \\ \rho_{ksqq} &= \sum_{\bar{n}} C_{\bar{n}}^*(t) C_{\bar{n}_{ks}^{qq}}(t) \sqrt{n_k n_s (n_q + 1)(n_q + 2)}, \quad \rho_{kssl} = \sum_{\bar{n}} C_{\bar{n}}^*(t) C_{\bar{n}_k^l}(t) n_s \sqrt{n_k(n_l + 1)}, \\ \rho_{ksql} &= \sum_{\bar{n}} C_{\bar{n}}^*(t) C_{\bar{n}_{ks}^{ql}}(t) \sqrt{n_k n_s (n_q + 1)(n_l + 1)}. \end{aligned}$$

Infinite resources for numerical calculation makes it possible to assume the theoretical limit  $M \rightarrow \infty$ , thus  $\hat{P} \rightarrow \hat{0}$  and  $\partial_t |\phi_j\rangle = 0$  in Eq. (S1), which means that a complete set of time-independent orbitals  $\{\phi_j(x) | j = 1, 2, \dots\}$  can be composed and the dynamics of systems is fully described only by the set of coefficients  $\{C_{\bar{n}}(t)\}$ , from which all quantum metrological properties can be extracted.

If  $M = 2$ , with fixed orbitals, is adequate for the description of a system, the modes comprise the conventional TMI, using a  $SU(2)$  formulation. Optical systems have been used to realize such two-mode systems, e.g., a Mach-Zehnder interferometer, where only the Fock space coefficients matter to predict the number of photons in each interferometric arm. However, for interacting atoms, an exact description requires infinite  $M$ , and truncating at finite  $M$  is valid only approximately, cf. the error-controlled extension of multiconfigurational Hartree put forth in [42]. As the interaction becomes weaker, a description in terms of finite  $M$  improves. The self-consistent MCTDH framework here goes significantly further than a conventional TMI and introduces time-evolving orbitals of changing shape. We also note here that a Hartree-Fock method, using plane waves for the field operator expansion as appropriate in a translationally invariant system, will fail to capture a trapped system when, as necessary for finite computational resources, the expansion is truncated at a finite  $M$ .

### Quantum Fisher information of a pure state in the MCTDH framework

Because of the introduction of time-evolving orbitals, a formulation of the QFI is required which facilitates incorporating the result of MCTDH time evolution by Eq. (S1). The QFI, which is the ultimate limit of precision given by  $|\psi_X\rangle$ , is calculated by  $\mathfrak{F}_X = 4(\langle \partial_X \psi_X | \partial_X \psi_X \rangle - |\langle \psi_X | \partial_X \psi_X \rangle|^2)$  for general pure states, and for some state represented as Eq. (1), we have, for any number of modes,

$$\begin{aligned} \mathfrak{F}_X/4 &= \sum_{\vec{n}} \partial_X C_{\vec{n}}^* \partial_X C_{\vec{n}} - \left| \sum_{\vec{n}} C_{\vec{n}}^* \partial_X C_{\vec{n}} \right|^2 \\ &+ \sum_{\vec{n}} \sum_{k,q} (\partial_X C_{\vec{n}}^* C_{\vec{n}_k^q} - C_{\vec{n}}^* \partial_X C_{\vec{n}_k^q}) (\partial_X)_{kq} \zeta_{qk} - \sum_{\vec{n}} (\partial_X C_{\vec{n}}^* C_{\vec{n}} - C_{\vec{n}}^* \partial_X C_{\vec{n}}) \sum_{k,q} (\partial_X)_{kq} \rho_{kq} \\ &- \sum_{k,s,q} (\partial_X)_{ks} (\partial_X)_{sq} \rho_{kq} + \left( \sum_{k,q} (\partial_X)_{kq} \rho_{kq} \right)^2 - \sum_{k,s,q,l} (\partial_X)_{kq} (\partial_X)_{sl} \rho_{ksql}, \end{aligned} \quad (\text{S4})$$

where  $\zeta_{qk} := \sqrt{n_k(n_q + 1)}$  or  $\zeta_{qk} := n_k$  if  $q \neq k$  or  $q = k$ , respectively, and  $(\partial_X)_{kq} := \int dx \phi_k^*(x, t) \partial_X \phi_q(x, t)$ . Refer to Eq. (S2) and Eq. (S3) for the definitions of  $\rho_{kq}$  and  $\rho_{ksql}$ . The first two terms involve only the coefficients and the remaining terms are related to the changes of coefficients and orbitals, for infinitesimal increment of  $X$ . In summary, Eq. (S4) completely incorporates the information orbitals as well as coefficients changing with  $X$ .

### Construction of the probability distribution in MCTDH for bosons

Here we explain how to construct the probability distribution of measurement outcomes. This process obviously depends on the specific systems and the choice of measurement. Here, the metrological implementation with the ultracold bosons trapped in a double-well potential is covered and the number of particles in each well is counted after the time evolution is finished, and considered as the measurement. The probability of a particle in  $\phi_j(x, t)$  to be found at the left ( $L$ ) or the right ( $R$ ) is defined as

$$P_{L,j} = \int_{-\infty}^0 |\phi_j(x, t)|^2 dx, \quad P_{R,j} = \int_0^{\infty} |\phi_j(x, t)|^2 dx, \quad (\text{S5})$$

where we assume that the center of the 1D potential is at  $x = 0$ .

Next, we need to consider the combinatorial problem related to many particles and bosonic statistics. Let us take for simplicity the example of  $N = 2$ . There are three measurement outcomes:  $\vec{n} := (n_L, n_R) = (2, 0)$ ,  $(1, 1)$ , and  $(0, 2)$ , in which  $n_L$  and  $n_R$  mean the numbers of particles found in the left well and in the right well, respectively. When the final state is  $\sum_{\vec{n}} C_{\vec{n}} |\vec{n}\rangle = \sum_{k=0}^2 C_k |2-k, k\rangle$ , the probability for each case is as follows:

$$\begin{aligned} P_0 &= P(\vec{n} = (2, 0)) = |C_0|^2 P_{L,1}^2 + |C_1|^2 P_{L,1} P_{L,2} + |C_2|^2 P_{L,2}^2, \\ P_1 &= P(\vec{n} = (1, 1)) = 2 |C_0|^2 P_{L,1} P_{R,1} + |C_1|^2 (P_{L,1} P_{R,2} + P_{R,1} P_{L,2}) + 2 |C_2|^2 P_{L,2} P_{R,2}, \\ P_2 &= P(\vec{n} = (0, 2)) = |C_0|^2 P_{R,1}^2 + |C_1|^2 P_{R,1} P_{R,2} + |C_2|^2 P_{R,2}^2, \end{aligned} \quad (\text{S6})$$

where it is trivial to show that  $P(\vec{n} = (2, 0)) + P(\vec{n} = (1, 1)) + P(\vec{n} = (0, 2)) = 1$  using  $P_{j,L} + P_{j,R} = 1$  and



$|C_0|^2 + |C_1|^2 + |C_2|^2 = 1$ . After careful inspection, one can rewrite the above probabilities as

$$\begin{aligned} P_0 &= P(\vec{\mathbf{n}} = (2, 0)) = \frac{|C_0|^2}{2} \begin{Bmatrix} P_{L,1} & P_{L,1} \\ P_{L,1} & P_{L,1} \end{Bmatrix} + \frac{|C_1|^2}{2} \begin{Bmatrix} P_{L,1} & P_{L,2} \\ P_{L,1} & P_{L,2} \end{Bmatrix} + \frac{|C_2|^2}{2} \begin{Bmatrix} P_{L,2} & P_{L,2} \\ P_{L,2} & P_{L,2} \end{Bmatrix}, \\ P_1 &= P(\vec{\mathbf{n}} = (1, 1)) = |C_0|^2 \begin{Bmatrix} P_{L,1} & P_{L,1} \\ P_{R,1} & P_{R,1} \end{Bmatrix} + |C_1|^2 \begin{Bmatrix} P_{L,1} & P_{L,2} \\ P_{R,1} & P_{R,2} \end{Bmatrix} + |C_2|^2 \begin{Bmatrix} P_{L,2} & P_{L,2} \\ P_{R,2} & P_{R,2} \end{Bmatrix}, \\ P_2 &= P(\vec{\mathbf{n}} = (0, 2)) = \frac{|C_0|^2}{2} \begin{Bmatrix} P_{R,1} & P_{R,1} \\ P_{R,1} & P_{R,1} \end{Bmatrix} + \frac{|C_1|^2}{2} \begin{Bmatrix} P_{R,1} & P_{R,2} \\ P_{R,1} & P_{R,2} \end{Bmatrix} + \frac{|C_2|^2}{2} \begin{Bmatrix} P_{R,2} & P_{R,2} \\ P_{R,2} & P_{R,2} \end{Bmatrix}, \end{aligned} \quad (\text{S7})$$

in which  $\{V\}$  means the permanent of a matrix  $V$ . By tracing the factor in front of each term and by considering bosonic statistics, one can find a regular pattern and generalize as follows:

$$P_j = P(\vec{\mathbf{n}} = (N - j, j)) = \frac{1}{N!} \binom{N}{j} \sum_{k=0}^N |C_k|^2 \{V_{j,k}\}, \quad (\text{S8})$$

where  $V_{j,k}$  is a special  $N \times N$  matrix, defined as below. The  $j$  is the number of particles in the right well, i.e.,  $\vec{\mathbf{n}} = (N - j, j)$  and the  $k$  means  $\vec{\mathbf{n}} = (N - k, k)$ . The example above shows how to compose the matrix  $V_{j,k}$ . In order to compose  $V_{1,2}$ , for example, “1” is represented as  $\{L, R\}$  and the “2” is represented as  $\{2, 2\}$ . The former is an ordered set of  $N - j$  of  $L$  and  $j$  of  $R$ , and the latter is a conversion of “how many particles there are in each mode” into an (ascending-)ordered set of the occupied mode numbers:

$$\begin{aligned} j = 0 : (2, 0) &\rightarrow \{L, L\}, & j = 1 : (1, 1) &\rightarrow \{L, R\}, & j = 2 : (0, 2) &\rightarrow \{R, R\}, \\ k = 0 : (2, 0) &\rightarrow \{1, 1\}, & k = 1 : (1, 1) &\rightarrow \{1, 2\}, & k = 2 : (0, 2) &\rightarrow \{2, 2\}. \end{aligned}$$

Then the former set makes up the row indices and the latter set makes up the column indices:

$$\begin{array}{c} 2 \ 2 \\ L \\ R \end{array} \rightarrow \begin{pmatrix} P_{L,2} & P_{L,2} \\ P_{R,2} & P_{R,2} \end{pmatrix} = V_{1,2}, \quad (\text{S9})$$

and its permanent is now readily obtained to be

$$\{V_{1,2}\} = \begin{Bmatrix} P_{L,2} & P_{L,2} \\ P_{R,2} & P_{R,2} \end{Bmatrix} = P_{L,2} P_{R,2} + P_{L,2} P_{R,2}. \quad (\text{S10})$$

For another example, let us suppose that  $N = 3$  and try to express  $V_{1,2}$ . The first subscript 1 is converted into  $\{L, L, R\}$  and the second one 2 is converted into  $\{1, 2, 2\}$ . Then

$$\begin{array}{c} 1 \ 2 \ 2 \\ L \\ L \\ R \end{array} \rightarrow \begin{pmatrix} P_{L,1} & P_{L,2} & P_{L,2} \\ P_{L,1} & P_{L,2} & P_{L,2} \\ P_{R,1} & P_{R,2} & P_{R,2} \end{pmatrix} = V_{1,2}, \quad (\text{S11})$$

and the permanent is  $\{V_{1,2}\} = 4P_{L,1}P_{L,2}P_{R,2} + 2P_{L,2}^2P_{R,1}$ . Now we have all ingredients to construct the probability distribution of a measurement for which the number of particles in each well is counted. To calculate the permanent of a matrix, we used the advanced algorithm developed in [43]; for an introduction see [44].

### More results on the implementation of the MLE

Here we supply some additional results on the MLE, see Fig. S1. The top left shows the mean of the maximum likelihood estimator with respect to the final state that has evolved under the true value of  $p_4$ . To calculate the mean, the probability distribution first needs to be composed. One measurement outcome is used at a single time of estimation, i.e.,  $\nu = 1$ . When the true value of  $p_4$  is 0.1,  $\langle X_{\text{est}} \rangle_X \simeq 0.0926$ . The top right plot shows the mean of the maximum likelihood estimator versus  $\nu$  when  $p_4 = 0.1$ , which is the number of measurement outcomes for a single estimation of  $p_4$ . As  $\nu$  increases,  $\langle X_{\text{est}} \rangle_X$  converges at around 0.11, which implies a bias of MLE. The bottom left

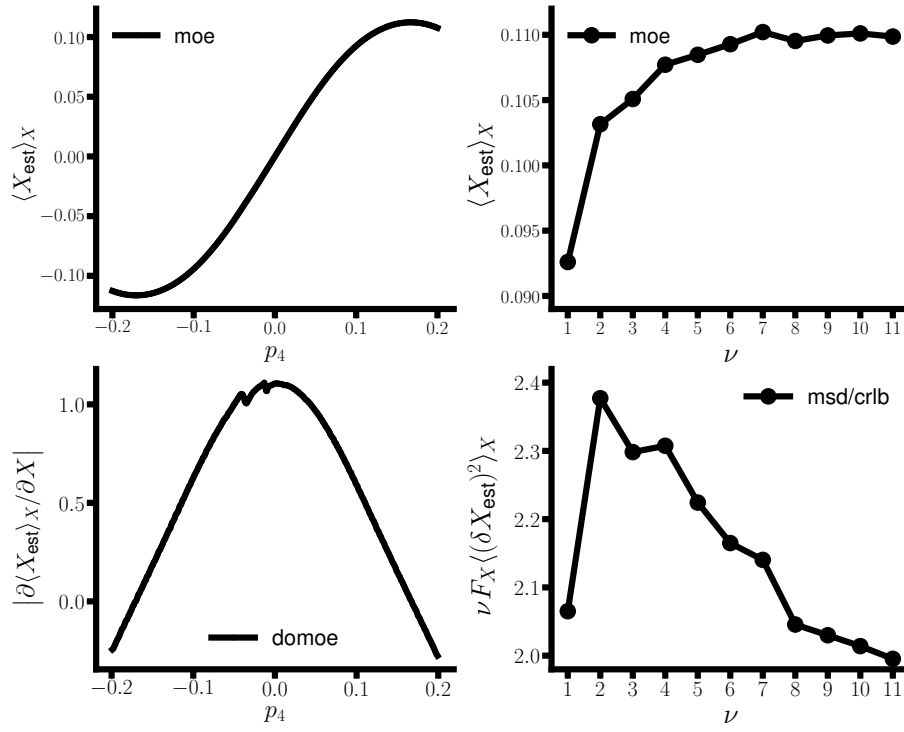


FIG. S1. Additional results on maximum likelihood estimation, where “moe” is the mean of estimates  $\langle X_{\text{est}} \rangle_X$ , “msd” is the mean-square deviation  $\langle (\delta X_{\text{est}})^2 \rangle_X$ , and “domoe” stands for the absolute value of the derivative of the mean of estimates  $|\partial \langle X_{\text{est}} \rangle_X / \partial X|$ .

shows this bias of the MLE, where  $|\partial \langle X_{\text{est}} \rangle_X / \partial X| \simeq 1$  near  $p_4 \simeq 0$ , which however does not hold as  $p_4$  deviates more significantly from zero. Lastly, the bottom right plot shows the ratio between the mean-square deviation and the Cramér-Rao lower bound (CRLB). This ratio decreases as  $\nu$  increases: The MLE is known to make the mean-square deviation  $\langle (\delta X_{\text{est}})^2 \rangle_X$  converge to the CRLB as  $\nu \rightarrow \infty$  according to the central limit theorem, which is thus confirmed herewith.